Increasing numerical stability of mountain valley glacier simulations: implementation and testing of free-surface stabilization in Elmer/Ice

André Löfgren[1], Thomas Zwinger[3], Peter Råback[3], Christian Helanow[1,2], and Josefin Ahlkrona[1,2]

[1]Department of Mathematics, Stockholm University, Sweden
[2]Swedish e-Science Research Centre, Sweden
[3]CSC — IT Center for Science Ltd, Espoo, Finland

Correspondence: André Löfgren (andre.lofgren@math.su.se)

Abstract. This paper concerns a numerical stabilization method for free-surface ice flow called the free-surface stabilization algorithm (FSSA). In the current study, the FSSA is implemented into the numerical ice-flow software Elmer/Ice and tested on synthetic two-dimensional (2D) glaciers, as well as on the real-world glacier of Midtre Lovénbreen, Svalbard. For the synthetic 2D cases it is found that the FSSA method increases the largest stable time-step size at least by a factor of ten for the case of a
5 gently sloping ice surface ($3°$), and by at least a factor of five for cases of moderately to steeply inclined surfaces ($6°$ to $12°$) . Furthermore, the FSSA method increases the overall accuracy for all surface slopes. The largest stable time-step size is found to be smallest for the case of a low sloping surface, despite having overall smaller velocities. For Midtre Lovénbreen the FSSA method doubles the largest stable time-step size, however, the accuracy is in this case slightly lowered in the deeper parts of the glacier, while it increases near edges. The implication is that the non-FSSA method might be more accurate at predicting
10 glacier thinning, while the FSSA method is more suitable for predicting future glacier extent. A possible application of the larger time-step sizes allowed for by the FSSA is for spin-up simulations, where relatively fast changing climate data can be incorporated on short time scales, while the slowly changing velocity field is updated over larger time scales.

1 Introduction

Ice sheets and glaciers are important constituents of the global climate system and the mass loss from these is expected to be
15 a main contributor to future sea-level rise (DeConto and Pollard, 2016; Hock et al., 2019; Meredith et al., 2019; Fox-Kemper et al., 2021). In order to reliably estimate future sea-level rise the accurate representation of ice-sheet and glacier dynamics is crucial, and higher-order physics models have proven to be instrumental in increasing the confidence in predictions (Hanna et al., 2013; Shepherd and Nowicki, 2017; Pattyn, 2018).

The most accurate description for the flow of ice, in the sense that all stress components are present in the Cauchy stress
20 tensor, are the Stokes equations (Greve and Blatter, 2009). Approximations to the model are made by neglecting various components, with some of the most notable examples being the shallow-ice approximation (SIA) (Hutter, 1983; Morland, 1984) and the first-order Stokes approximation (FOS) (Blatter, 1995; Pattyn, 2003). Owing to its simplicity and computational

efficiency, the SIA method has a long history of use (see e.g., Blatter et al., 2010, for a historical overview); however, the SIA method has been found to be insufficient at reproducing the flow at regimes with a steep sloping bedrock (Meur et al., 2004; Dukowicz et al., 2011; Leng et al., 2012), as well as for smaller glaciers with a complex bedrock topography (Zwinger et al., 2007).

It has been demonstrated for lower-order physics models, such as SIA, that when coupled to the free-surface equation governing the evolution of ice sheets and glaciers they suffer from a parabolic type time-step size constraint that is highly dependent on the ice-domain thickness (Bueler et al., 2005; Gong et al., 2017; Bueler, 2022; Robinson et al., 2022). However, for the Stokes equations the same parabolic time-step size restriction does not necessarily hold true — even for setups where the SIA and the Stokes equations gives qualitatively similar solutions (Löfgren et al., 2022). Still, for ice-sheet simulations using the Stokes equations, the time-step sizes complying with the stability restrictions are typically found to be in the order of 0.1 to 10 yr (Gong et al., 2017; Löfgren et al., 2022). This is considerably smaller than typical time-scales at which ice-sheets evolve (Hindmarsh and Payne, 1996), which can be as large as 10000 yr (Greve and Blatter, 2009). Computation times can thus be cut if time-step sizes can be increased beyond the largest stable time-step size (LST) without compromising the desired accuracy of the solution.

One way of stabilizing the problem is to use a fully implicit time-stepping scheme, which has been demonstrated by Bueler (2016) for the SIA in a frozen-bed setting. However, the Stokes equations are considerably more expensive to solve than the simpler SIA equations and, since the nonlinear Stokes equations would have to be solved multiple times in each time step, makes such a scheme computationally infeasible for long-term simulations. Instead Kaus et al. (2010) propose the free-surface stabilization algorithm (FSSA) which modifies the weak formulation of the Stokes equations in order for the free-surface coupled system to mimic an implicit time-stepping scheme. The method was originally developed for mantle-convection simulations where a similar viscous-flow problem is solved, and multiple studies have indeed demonstrated that the method lengthens the LST substantially (Kaus et al., 2010; Duretz et al., 2011; Kramer et al., 2012; Andrés-Martínez et al., 2015; Rose et al., 2017).

From a glaciological perspective, a limitation of the original FSSA method is that linear rheologies are used on domains that are geometrically isotropic, meaning that they span equally in horizontal and vertical directions; i.e., domain aspect ratios are 1:1. A notable exception is Glerum et al. (2020), which considers both a similar shear-thinning nonlinear rheology and domains with aspect ratios in the order of 1:10. Still, the values of the physical parameters describing ice flow are different from that in mantle convection, and aspect ratios of ice sheets can be as small as 1:1000.

These issues were addressed by Löfgren et al. (2022), where the FSSA method was adapted to ice-flow modeling. It was concluded that the method works well in an ice-dynamical setting, and for the problems presented showed the potential to increase the LST by an order of magnitude. Nevertheless, one of the shortcomings in this case is that the method was only applied to simple ice-sheet benchmark problems, and more complex glacier simulations and real-world applications were not considered and left for future studies.

This work focuses on addressing these issues and applying the FSSA method to the regime of glacier modeling, considering both slip conditions and steep bedrock and surface inclinations. The method is assessed with regards to stability and accuracy
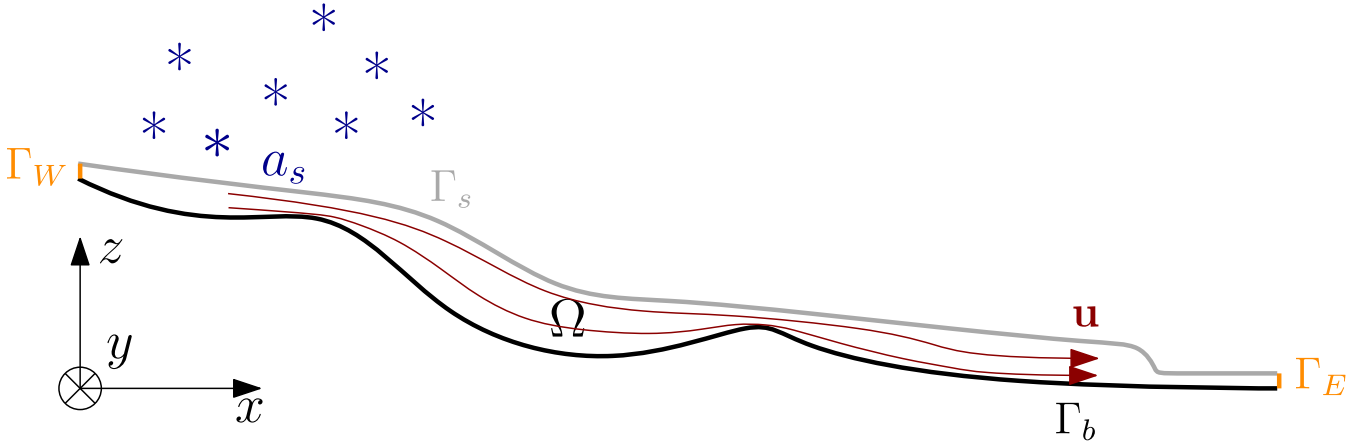
Figure 1. Cross section of a generic glacier domain Ω with its bedrock, Γ_b, marked in black and its surface, Γ_s, marked in gray. The west, Γ_W, and east, Γ_E, sides are marked in orange. The dark-red lines in the interior are the flow lines of the velocity field $\mathbf{u}$, and a_s is the accumulation/ablation rate.

for a synthetic case in two dimensions (2D) with a random-generated bedrock topography, using a novel method based on so-called Perlin noise (Perlin, 1985) and a real-world application to the glacier of Midtre Lovénbreen, Svalbard. The experiments are carried out using the ice-sheet solver Elmer/Ice (Gagliardini et al., 2013), where the FSSA method has been implemented.

The rest of the paper is structured as follows: in Sect. 2 the equations governing the flow of ice are presented; Sect. 3 introduces the numerical methods, including a presentation of the FSSA method for ice-sheet and glacier simulations; in Sect. 4, the experiments are presented along with their results; and finally the paper is concluded in Sect. 5 with a discussion of the results and the general outlook of the FSSA method from the perspective of glacier modeling.

2 Governing equations

2.1 The Stokes equations

The dynamics of ice flow can be described as a very slow-moving gravity-driven highly viscous fluid and is as such governed by the Stokes equations, see e.g., Greve and Blatter (2009)

$$\nabla \cdot (2\eta(\mathbf{u})\dot{\varepsilon}(\mathbf{u})) - \nabla p = \rho g \hat{\mathbf{z}}, \quad \mathbf{x} \in \Omega, \tag{1}$$

$$\nabla \cdot \mathbf{u} = 0, \quad \mathbf{x} \in \Omega, \tag{2}$$

where Eq. (1) follows from conservation of momentum and Eq. (2) from the conservation of mass. Furthermore, $\dot{\varepsilon} = \frac{1}{2}\left(\nabla\mathbf{u} + \nabla\mathbf{u}^T\right)$ is the strain-rate tensor, $\mathbf{u}$ and p are the ice velocity and pressure, respectively, at spatial coordinate $\mathbf{x}$ in the domain $\Omega \subset \mathbb{R}^d$ (see Fig. 1), where $d \in \{2,3\}$ is the geometrical dimension. Furthermore, $\rho = 917 \text{ kg m}^{-3}$ is the ice density and $g = 9.8 \text{ m/s}^2$ is the acceleration due to gravity. Lastly, η is the effective viscosity, which for ice depends on the velocity and temperature

75 through Glen's flow law (Glen, 1955; Nye, 1957)

$$\eta(\mathbf{u}, T') = A(T')^{-\frac{1}{n}} \left(\frac{1}{2} tr(\dot{\varepsilon}^2) + \dot{\varepsilon}_0^2 \right)^{\frac{1-n}{2n}}. \tag{3}$$

Here $n = 3$ (Cuffey and Paterson, 2010) is the Glen or power-law exponent and $\dot{\varepsilon}_0^2 = 10^{-10}$ yr^{-2} is a small regularization term added in order to avoid an infinite viscosity at zero strain rates. The rate factor $A(T')$ depends on the ice temperature relative to the pressure melting point T' through the Arrhenius equation (Glen, 1955)

80 $$A(T') = A_0 \exp\left(-\frac{Q}{RT'} \right), \tag{4}$$

where $A_0 = 2.89165 \times 10^{-13}$ s^{-1} Pa^{-3} is a pre-exponential factor, $Q = 60$ kJ mol^{-1} is the activation energy and $R = 8.314462$ JK^{-1}mol^{-1} is the ideal gas constant. The values stated here are the ones recommended by Paterson (1994) for ice at a temperature $T' \geq -10°$ C when $n = 3$.

2.2 Boundary conditions

85 In order to specify appropriate boundary conditions (BC), the glacier boundary, $\partial\Omega$, is divided into non-overlapping boundary parts Γ_s, Γ_W, Γ_b and Γ_E, see Fig. 1. The ice surface Γ_s is the only non-stationary part of the domain, meaning the future of the glacier is determined purely by the evolution of the surface. For the different parts of the boundary, the following BCs are considered

$$\sigma\hat{\mathbf{n}} = \mathbf{0}, \quad \mathbf{x} \in \Gamma_s, \tag{5}$$

90 $$\mathbf{u} \cdot \hat{\mathbf{n}} = 0, \quad \mathbf{x} \in \partial\Omega / \Gamma_s, \tag{6}$$

$$\hat{\mathbf{t}}_i \cdot \sigma\hat{\mathbf{n}} = -\beta^2 |\mathbf{u}|^{m-1} \mathbf{u} \cdot \hat{\mathbf{t}}_i, \quad \mathbf{x} \in \Gamma_b^s, \tag{7}$$

$$\mathbf{u} = \mathbf{0}, \quad \mathbf{x} \in \Gamma_b^f, \tag{8}$$

where $\sigma = 2\eta\dot{\varepsilon} - pI$ (I is the identity matrix) is the Cauchy stress tensor, $\hat{\mathbf{n}}$ is the unit normal outward pointing to the boundary, $\{\hat{\mathbf{t}}_i\}_{i=0}^{d-1}$ are tangent vectors spanning the plane defined by $\hat{\mathbf{n}}$, β is the drag coefficient, and $m \geq 1$ is an exponent.

95 The explanation of each BC is as follows: Eq. (5), is a stress-free condition on the glacier surface, following from the assumption that the stresses asserted on the surface due to, for instance, wind or the atmospheric pressure are negligible compared to the internal stresses (Greve and Blatter, 2009). The second BC, Eq. (6), is an impenetrability condition under which ice cannot flow into the bedrock, meaning its velocity in the direction normal to the bedrock must necessarily be zero. The third BC, Eq. (7), is a Weertman-type sliding law (Weertman, 1957), stating that the ice may slip along the bedrock, following a power law relation between the slip velocity and the shear stress. This study focuses only on the case for which

100 $m = 1$, such that the relation is linear. Lastly, the fourth BC, Eq. (8), is a no-slip BC representing conditions where the ice is frozen to bedrock. The bedrock thus consists of parts, Γ_b^s, where slip is present and parts, Γ_b^f, where no slip occurs.

2.3   The free-surface equation

The time evolution of a glacier (or an ice sheet) is determined by its surface position $z_s = z_s(x, y, t)$ and is governed by a

105   separate equation called the free-surface equation (Greve and Blatter, 2009)

$$\frac{\partial z_s}{\partial t} + u_x^s \frac{\partial z_s}{\partial x} + u_y^s \frac{\partial z_s}{\partial y} = u_z^s + a_s, \tag{9}$$

where a_s is the vertical rate of mass accumulation (or ablation), $\mathbf{u}^s = (u_x^s, u_y^s, u_z^s)$ is the velocity field from the Stokes equations
Eq. (1) - (2) evaluated on the surface boundary Γ_s, see Fig. 1.

3   Computational aspects

3.1   Solution procedure

The time-stepping approach for solving the Stokes equations coupled to the free-surface equation is shown in Fig. 2a and
consists of first solving the Stokes equations, Eq. (1) - (2), for the velocity field evaluated on the surface, $\mathbf{u}^s$, which then
enters as coefficients into the free-surface equation, Eq. (9). The free-surface equation is then solved for a new height function,
$z_s(x, y, t + \Delta t)$, which in turn determines the new domain $\Omega(t + \Delta t)$. The mesh is updated based on an extruded-mesh principle,

115   wherein nodes are vertically aligned in columns such that the mesh can be updated by simply displacing nodes vertically
according to the new height function $z_s(x, y, t + \Delta t)$; see e.g., Löfgren et al. (2022) for implementation details. This process is
repeated until the final simulation time is reached. This is the standard approach in ice-sheet modeling (used in e.g., Elmer/Ice
Gagliardini et al., 2013), and is in this study referred to as an explicit time-stepping scheme in terms of velocity.

   The explicit time-stepping scheme can be contrasted with the implicit time-stepping scheme (in terms of velocity) in Fig. 2b,

120   where an extra loop is needed in order to the resolve the velocity field $\mathbf{u}(t + \Delta t)$ over the next time step. This has the disadvan-
tage that the computationally expensive nonlinear Stokes equations need to be solved repeatedly in each time step, by iterating
back- and forth between the domain at the old time step $\Omega(t)$ and the domain at the new time step $\Omega(t + \Delta t)$. The advantage is
that it is numerically stable, allowing for large time-step sizes. The goal of this paper is to evaluate an approach, the FSSA, that
finds a solution which is close to the solution yielded by the implicit time-stepping scheme without adding the extra computa-

125   tionally costly iteration. It is thus an approach that uses the explicit time-stepping scheme in a way that is stable and without
substantial loss of accuracy.

3.2   The Stokes weak formulation - the basis for the stabilization method

The Stokes equations, Eq. (1) - (2), are discretized and solved numerically using the finite element method (FEM), which
requires to first recast the problem in its weak form: Find $(\mathbf{u}, p) \in \mathcal{X} \times \mathcal{Q}$ such that

130   $(\dot{\varepsilon}(\mathbf{v}) : 2\eta \dot{\varepsilon}(\mathbf{u}))_\Omega - ((\nabla \cdot \mathbf{v}) p)_\Omega - (q \nabla \cdot \mathbf{u})_\Omega + (\beta^2 \mathbf{v} \cdot \mathbf{u})_{\Gamma_b} = -(\rho g \mathbf{v} \cdot \hat{\mathbf{z}})_\Omega, \tag{10}$
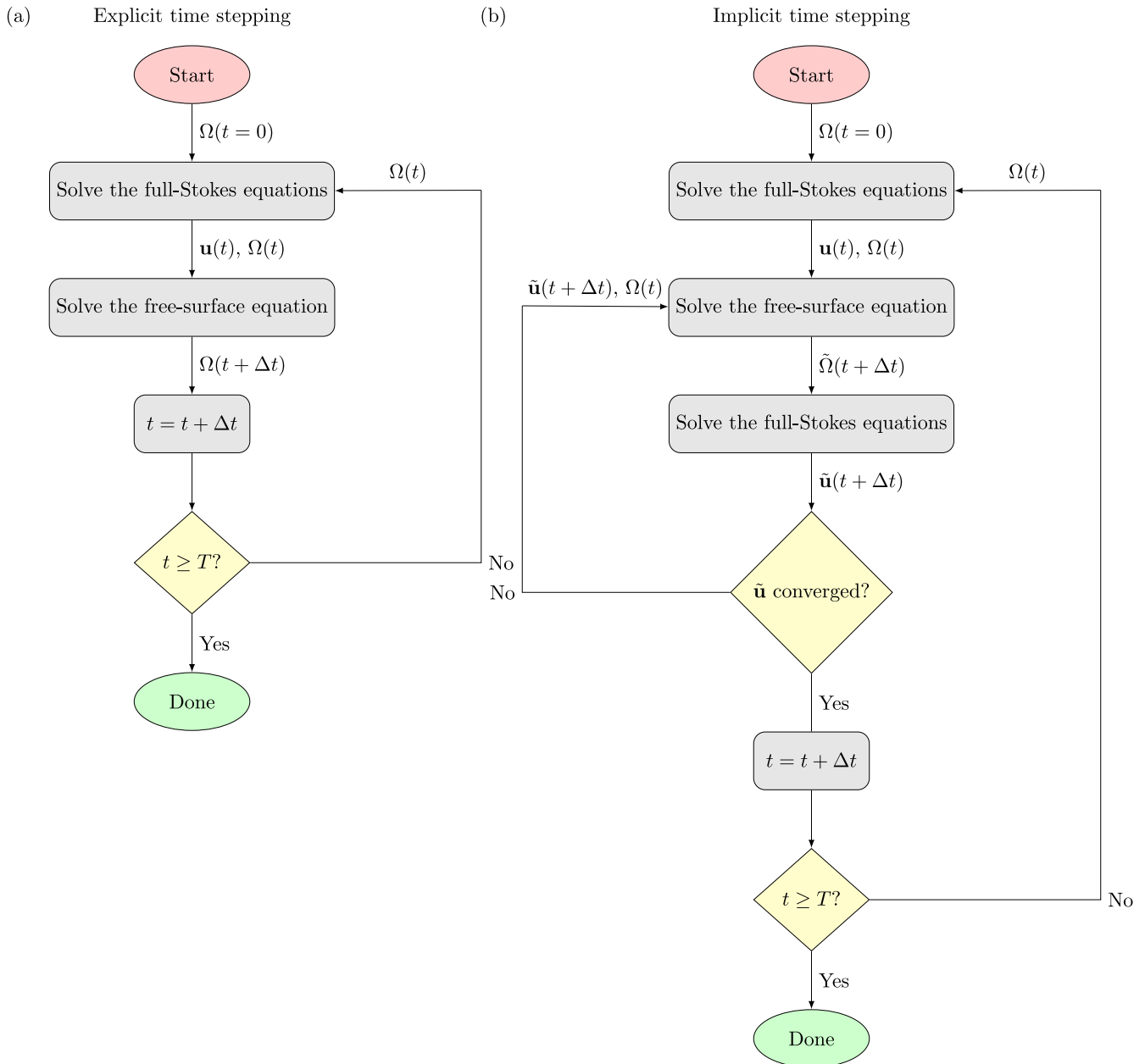
Figure 2. Explicit (a) and implicit (b) time-stepping schemes. For each time step the explicit scheme solves the Stokes equations, Eq. (1) - (2), for the velocity field $\mathbf{u}(t)$ on the domain of the current time step $\Omega(t)$, the solution $\mathbf{u}(t)$ then enters as a coefficient into the free-surface equation, Eq. (9), from which the domain at next time step, $\Omega(t + \Delta t)$, is obtained directly and the time is updated, i.e., $t = t + \Delta t$. The implicit scheme on the other hand solves for velocity at the next time step $\mathbf{u}(t + \Delta t)$. The procedure for obtaining $\mathbf{u}(t + \Delta t)$ is as follows: in each time step the Stokes equations are solved for $\mathbf{u}(t)$, which is then inserted into the free-surface equation to obtain an estimate of the new domain $\tilde{\Omega}(t + \Delta t)$. The Stokes equations are then solved on $\tilde{\Omega}(t + \Delta t)$ to obtain an estimate $\tilde{\mathbf{u}}(t + \Delta t)$. This estimate is then evaluated if it is close to the velocity field $\mathbf{u}(t + \Delta t)$, given some estimate of the convergence. If the estimate is not close, the process is repeated until convergence is obtained. Finally, after convergence, the time is updated. For both cases the algorithm terminates when the final simulation time, T, is reached.

for all $(\mathbf{v}, q) \in \mathcal{X} \times \mathcal{Q}$. Here $(\cdot)_\Omega = \int_\Omega \cdot d\Omega$, the Frobenius inner product is represented by the colon operator (:), and $\mathcal{X}$ and $\mathcal{Q}$ are appropriate function spaces. The integrals and the fact that the forcing term is constant opens up for the construction of the FSSA method, as will be described in the next section.

The nonlinear nature of this system (Eq. (10)) requires linearizing the viscous term with Picard or Newton iterations. Convergence issues sometimes prohibit using Newton solvers for glaciological problems. To overcome these issues, new relaxation methods are introduced in Elmer/Ice (see Sect. 4.3).

3.3 Free surface time discretization and stabilization

To discretize the free-surface equation, Eq. (9), in time, a semi-implicit Euler discretization is employed, such that

$$z_s^{k+1} + \Delta t \left(u_x^k \frac{\partial z_s^{k+1}}{\partial x} + u_y^k \frac{\partial z_s^{k+1}}{\partial y} \right) = z_s^k + \Delta t \left(u_z^k + a_s^k \right) \tag{11}$$

where Δt is the time-step size and z_s^{k+1} is the unknown surface at time step $k+1$ to be solved for (here k denotes the time step). The scheme is called semi-implicit since it is implicit in terms of the surface z_s and explicit in terms of velocity $\mathbf{u}$.

The explicit nature of the time-stepping scheme in Eq. (11) makes it prone to numerical instabilities. A fully implicit scheme would, on the other hand, involve a highly expensive computation in order to evaluate $\mathbf{u}^{k+1}$, see Fig. 2b. To circumvent this problem, the FSSA was introduced by Kaus et al. (2010) for mantle-convection problems and adapted to glaciological problems in Löfgren et al. (2022). The FSSA mimics a fully implicit scheme by estimating the impact of the force of gravity over the new domain, Ω^{k+1}, following Reynold's transport theorem. The standard form of Reynolds transport theorem is (see e.g., Greve and Blatter, 2009)

$$\frac{d}{dt} \int\limits_{\Omega(t)} f \, d\Omega = \int\limits_{\Omega(t)} \frac{\partial}{\partial t} f \, d\Omega + \int\limits_{\partial\Omega(t)} (\mathbf{u}_b \cdot \hat{\mathbf{n}}) f \, d\Gamma, \tag{12}$$

where $\mathbf{u}_b$ is the velocity of the moving boundary and f some scalar-valued function. In the case considered $f = -\rho g \hat{\mathbf{z}} \cdot \mathbf{v}$, which is constant in time and therefore results in the first term on the left-hand side of Eq. (13) to be zero. In Eq. (13) the domain is assumed to move only due to the velocity of deformation. In ice-sheet modeling, however, the ice surface also moves due to accumulation and ablation, a_s. Taking this into account gives the estimate of the forcing on the time step $k+1$ as

$$(\rho g \mathbf{v} \cdot \hat{\mathbf{z}})_{\Omega^{k+1}} \approx (\rho g \mathbf{v} \cdot \hat{\mathbf{z}})_{\Omega^k} + (\rho g \Delta t (\mathbf{v} \cdot \hat{\mathbf{z}}) ((\mathbf{u} + a_s \hat{\mathbf{z}}) \cdot \hat{\mathbf{n}}))_{\Gamma_s^k}. \tag{13}$$

Here the factor $(\mathbf{u} + a_s \hat{\mathbf{z}}) \cdot \hat{\mathbf{n}}$ is an approximation of the change of the domain from time step k to $k+1$. Note how the integrals of the weak form and the fact that ρg is constant are features that opens up for using Reynolds transport theorem in this simple way. Inserting Eq. (13) into the Stokes weak formulation Eq. (10) yields the FSSA stabilized weak formulation appropriate for glaciology: Find $(\tilde{\mathbf{u}}^{k+1}, \tilde{p}^{k+1}) \in \mathcal{X} \times \mathcal{Q}$ such that

$$(\dot{\varepsilon}(\mathbf{v}) : 2\eta \dot{\varepsilon}(\tilde{\mathbf{u}}^{k+1}))_{\Omega^k} - ((\nabla \cdot \mathbf{v})\tilde{p}^{k+1})_{\Omega^k} - (q \nabla \cdot \tilde{\mathbf{u}}^{k+1})_{\Omega^k} + (\beta^2 \mathbf{v} \cdot \tilde{\mathbf{u}}^{k+1})_{\Gamma_b^k} + (\rho g \theta \Delta t (\mathbf{v} \cdot \hat{\mathbf{z}})(\mathbf{u} \cdot \hat{\mathbf{n}}))_{\Gamma_s^k}$$
$$= -(\rho g \mathbf{v} \cdot \hat{\mathbf{z}})_{\Omega^k} - (\rho g \theta \Delta t a_s (\mathbf{v} \cdot \hat{\mathbf{z}})(\hat{\mathbf{n}} \cdot \hat{\mathbf{z}}))_{\Gamma_s^k}, \tag{14}$$

160   for all $(\mathbf{v}, q) \in \mathcal{X} \times \mathcal{Q}$. Here $\theta \in \mathbb{R}^+$ is a stabilization parameter governing the implicitness of the solver, in particular $\theta = 0$ corresponds to a fully explicit solver and $\theta = 1$ fully quasi-implicit. The solution $\tilde{\mathbf{u}}^{k+1}$ is an approximation of the solution $\mathbf{u}^{k+1}$ obtained from the fully implicit scheme. The validity of the FSSA approximation follows from the fact that the gravitational force is driving the ice flow.

     To better understand the effect of the stabilization term, insight can be gained by applying the FSSA to the SIA approximation

165   of the Stokes equations, for which it can be shown that (see the appendix in Löfgren et al. (2022))

$$p \approx \rho g(z_s^k - z) + \theta \Delta t (u_x, u_z) \cdot \hat{\mathbf{n}}(-\rho g) = \rho g(z_s^k - z) - \theta \rho g\left(z_s^k - z_s^{k+1}\right) = \rho g((1-\theta)z_s^k + \theta z_s^{k+1} - z). \tag{15}$$

For $\theta = 1$ this results in $p \approx \rho g(z_s^{k+1} - z)$. Since the pressure is determining the SIA velocity, this means that the velocity is calculated using z_s^{k+1} instead of z_s^k.

4   Numerical experiments

170   **4.1   Overview**

In this section two experiments using varying bedrock slopes and sliding conditions are presented to demonstrate the applicability of the FSSA method to glacier modeling and to assess its stabilizing properties. In the first experiment, the method is applied to a 2D flow-line case, with an undulating bedrock generated using gradient noise (see Appendix A), superimposed on a sloping bedrock. The FSSA method is investigated with regards to accuracy and stability for different bedrock slopes. The

175   second experiment applies the FSSA method to the real-world glacier of Midtre Lovénbreen, Svalbard, and is evaluated based on stability and accuracy.

4.2   Experiment 1: 2D "Perlin" Glacier

4.2.1   Setup

This experiment consists of a 2D glacier geometry with a sloping, undulating bedrock, where accumulation and sliding condi-

180   tions are present. The bedrock is generated by superimposing three gradient-noise octaves on a parabola, such that

$$z_b(x) = \frac{\alpha}{L_x}(x - L_x)^2 + C^1 \text{octave}_1(\Delta x^1, x) + C^2 \text{octave}_2(\Delta x^2, x) + C^3 \text{octave}_3(\Delta x^3, x) \tag{16}$$

where α is the average slope, $L_x = 8000$ m is the horizontal extent of the domain and the octaves represent noise of different frequencies (see Appendix A). The coefficient of the parabola has been chosen such that $\frac{dz_b}{dx}(0) = 2\alpha$ and $\frac{dz_b}{dx}(L_x) = 0$. The noise amplitudes are set to $C^1 = 300$ m, $C^2 = 500$ m and $C^3 = 600$ m and the respective octave frequencies to $\Delta x^1 = 2000$

185   m, $\Delta x^2 = 1000$ m and $\Delta x^3 = 500$ m. The resulting bedrocks are visible in Fig 3.

     The initial ice surface is a thin layer of ice

$$z_s(x, 0) = z_b(x) + H_{min}, \tag{17}$$

where $H_{min} = 10$ m. To build up a glacier on the bedrock, a non-negative accumulation function that is linearly decaying (with the horizontal coordinate) with a maximum at $x = 0$ is used:

$$a(x) = max\left(1 - \frac{3x}{L_x}, 0\right). \tag{18}$$

The BCs imposed are impenetrability, Eq. (6), on the west- and east boundaries, Γ_W and Γ_E (see Fig. 1). On the surface Γ_s, the free-surface condition Eq. (5) is applied. Lastly, on the bedrock, Γ_b, the impenetrability BC, Eq. (6), is combined with the linear Weertman sliding law of Eq. (7), with a drag coefficient given by

$$\beta^2(x) = \beta_{min}^2 + \frac{\beta_{max}^2 - \beta_{min}^2}{1 + \exp\left(\frac{x-\mu}{\sigma}\right)}, \tag{19}$$

where $\beta_{max}^2 = 1000$ MPa yr m^{-1}, $\beta_{min}^2 = 0.01$ MPa yr m^{-1}, $\sigma = 200$ m and $\mu = 3000$ m. This drag coefficient should be viewed as a transition from a no-slip condition when $x \ll \mu$ to a free-slip condition when $x \gg \mu$, with the length of the transition zone controlled by σ.

To investigate how accuracy and stability properties of the FSSA method are influenced by increasing bedrock slopes, simulations are performed on three domains with different average bedrock slopes in Eq. (16): $\alpha = 0.05$ ($\approx 2.9°$) (gently sloping glacier), $\alpha = 0.1$ ($\approx 5.7°$) (moderately sloping glacier) and $\alpha = 0.2$ ($\approx 11.5°$) (steep sloping glacier). To estimate the error, a reference solution is obtained for all three cases by performing simulations using a fine time-step size $\Delta t = 0.05$ yr and a fine mesh resolution with $(N_x, N_z) = (1000, 10)$, where N_x and N_z are the number of layers in the horizontal- and vertical directions, respectively. The motivation behind using a finer spatial discretization for the reference solution is to ensure that spatial errors remain small compared to temporal errors, given the small time-step size, as spatial errors can accumulate in each time step. The reference simulations are performed until final times $t = 900$ yr, $t = 700$ yr and $t = 500$ yr, for the respective cases.

Subsequent coarse mesh simulations, $(N_x, N_z) = (400, 5)$, are then started from an intermediate glacier surface obtained from the reference simulation, starting from times $t = 500$, yr $t = 400$ yr, and $t = 300$ yr. The error is then estimated by comparing the ice thickness, $H(x) = z_s(x) - z_b(x)$, of the coarse mesh solutions to the thickness of the reference simulation, H_{ref}, at the final times for the respective slopes. The ice thickness error ϵ_H is computed as

$$\epsilon_H = \frac{||H_{ref} - H||_2}{||H_{ref}||_2}, \tag{20}$$

where $||\cdot||_2$ denotes the discrete L2-norm. The error is then measured for multiple coarse mesh simulations, with and without FSSA, for various time-step sizes Δt.

Following Gong et al. (2017) and Löfgren et al. (2022), all simulations use a constant rate factor $A = 100$ yr^{-1}MPa^{-3} in Eq. (3) and a constant ice density $\rho = 910$ kg m^{-3}.

4.2.2   Results

The reported stability and estimated ice thickness error, ϵ_H, as calculated by Eq. (20), are shown in Table 1 for different bedrock slopes α and FSSA stabilization parameters θ. The FSSA method ($\theta = 1$) is found to be stable for all tested time-step sizes, up

to $\Delta t = 50$ yr, while for $\theta = 0$ the largest stable time-step size (LST) is between 5 to 10 yr for $\alpha = 0.05$ and between 10 to 25

220   yr for $\alpha = 0.1$ and $\alpha = 0.2$. The FSSA method thus increases the LST by at least a factor of two for all cases, and may even be as large as ten times for $\alpha = 0.05$ and five times as large for $\alpha = 0.1$ and $\alpha = 0.2$. Compared to ice-sheet simulations in e.g., Löfgren et al. (2022) the time-step sizes are large even without stabilization.

The LST is larger for the steep bedrock case, despite the velocity field also having a larger magnitude (see Fig. 3d–f). The reason for this might be related to the low and moderately inclined bedrock cases having a greater ice thickness, for which

225   analytical expressions derived using zeroth-order approximation, e.g., SIA, have shown a strong inverse relation between the LST and the ice thickness (Gong et al., 2017; Robinson et al., 2022). In Löfgren et al. (2022) it was shown that the characteristics of the instabilities for Stokes-coupled free-surface flow are related to the domain aspect ratio: thicker domains tend to give rise to long wavelength sloshing instabilities, while thin domains give rise to numerical oscillation of shorter wavelengths.

230   In the current experiment, thick domains are represented by $\alpha = 0.05$ and $\alpha = 0.1$ where velocities are low enough for a thicker ice to develop, and the thin domain is represented by $\alpha = 0.2$. Indeed from Fig. 4, which shows a time series of vertical velocity profiles for unstable time-step sizes, it is seen that for low and moderate bedrock slopes, Fig. 4a–c and Fig. 4d–f, respectively, the instabilities behave differently than for the case of a steep bedrock, Fig 4g–i. In the former cases the instabilities emerge as result of the vertical velocity profiles shifting in sign and growing in magnitude between time steps,

235   resulting in the glacier surface sloshing around the stable reference surface (black dashed lines in Fig 4). For the steep bedrock case, while sloshing is possible to discern in the interior, the most prominent feature of the instabilities are the high frequency numerical oscillations occurring at the glacier front, seen in Fig. 4i. Despite the different characteristic of the instabilities arising for the different cases, it is clear from Table 1 and Fig. 3 that the FSSA method mitigates instabilities in both cases, as was also concluded by Löfgren et al. (2022).

240   Comparing the errors of the FSSA method ($\theta = 1$) to no stabilization ($\theta = 0$) in Table 1, it is seen that the FSSA method generally yields a much more accurate solution. The exception being for small time-step sizes Δt, where the error for the FSSA method is just slightly smaller. However, as Δt increases, the discrepancy in the error between the methods grows with the error being smaller for the FSSA method. For $\Delta t \geq 2.5$ yr the error for all slopes is almost twice as large when $\theta = 0$ compared to $\theta = 1$. For some cases, even using a twice as large time-step size with FSSA compared to no FSSA, the increase in the error

245   is much less than the expected 100 %.

Generally, the error increases linearly with the time-step size Δt, i.e., $\epsilon_H = \mathcal{O}(\Delta t)$, as is expected of the semi-implicit Euler time-stepping scheme in Eq. (11). This observation holds regardless of the slope α and stabilization parameter θ. An exception is, however, seen for the smaller time-step sizes ($\Delta t \leq 1$) where the error remains relatively unchanged between the refinement from $\Delta t = 1$ yr to $\Delta t = 0.5$ yr. This is expected for sufficiently small Δt, and may indicate that the temporal error is of the

250   same order as the spatial error when $\Delta t \approx 1$ yr, such that further refinement of the time-step size does not improve the accuracy of the coarse mesh solution.

Figure 3 shows the glacier surfaces at the final times for different Δt and θ. In all cases it is seen from the zoom-in plots that a too large time-step size gives a too thin glacier front, compared to the reference solution. Comparing Table 1 and Fig. 3,

it is seen that a larger error corresponds to a thinner glacier front. Consequently, the FSSA method, which is generally more

255 accurate in this experiment, yields a faster moving front for the same Δt. This is expected based on the fact that the FSSA method is a quasi-implicit time-stepping scheme, meaning it uses an estimate of the velocity from the next time step to update the glacier surface in Eq. (9). Since the glacier is growing in size, the velocity field is expected to increase in magnitude over the duration of the simulation, such that $||\mathbf{u}^{k+1}|| \geq ||\mathbf{u}^k||$ (k denotes the time step), meaning that the FSSA method gives a larger velocity coefficient in the free-surface equation, and thus yields a faster moving front.

260 The error also increases with the bedrock slopes α, despite the simulation times being shorter, which is expected given that larger slopes give a higher velocity coefficient in the free-surface equation, Eq. (9). From the large error seen for the steep bedrock case, $\alpha = 0.2$, it is not even clear that stability considerations are the limiting factor for the time-step size, it might as well in practical applications come down to accuracy — depending on whether Eq. (20) is deemed a satisfactory error metric. From a practical point of view, this has the implication that using a time-step size close to the LST may not be a wise strategy

265 when employing the FSSA method as the error in the final ice thickness is quite large for, e.g., the stable case of $\Delta t = 50$ yr, especially for the long term simulations considered in this experiment. On the other hand, the smaller errors observed for $\alpha = 0.05$ and $\alpha = 0.1$, indicates that stability considerations are more important for the time-step size. Thus, for a given error tolerance, the FSSA method seems to offer the greatest potential for speed-up for simulating glaciers that are on top of bedrocks with a topography that is gently to moderately inclined. Regardless of surface slope, it is obvious that the FSSA method gives

270 not only a more stable solver, but also increases its accuracy.

In summary, the main finding is that the FSSA method allows for using larger time-step sizes by increasing both accuracy and stability, for all slopes angles investigated. However, the method seems to offer the greatest benefit for low to moderately sloping glaciers, where the time-step size seems to be mainly limited by stability considerations.

Table 1. Relative error in the ice thickness, as defined by Eq. (20), for different time-step sizes Δt and bedrock slopes α. The error is calculated after final times 900 yr, 700 yr and 500 yr for the respective slopes $\alpha = 0.05$, $\alpha = 0.1$ and $\alpha = 0.2$. Entries marked with an X are unstable cases.

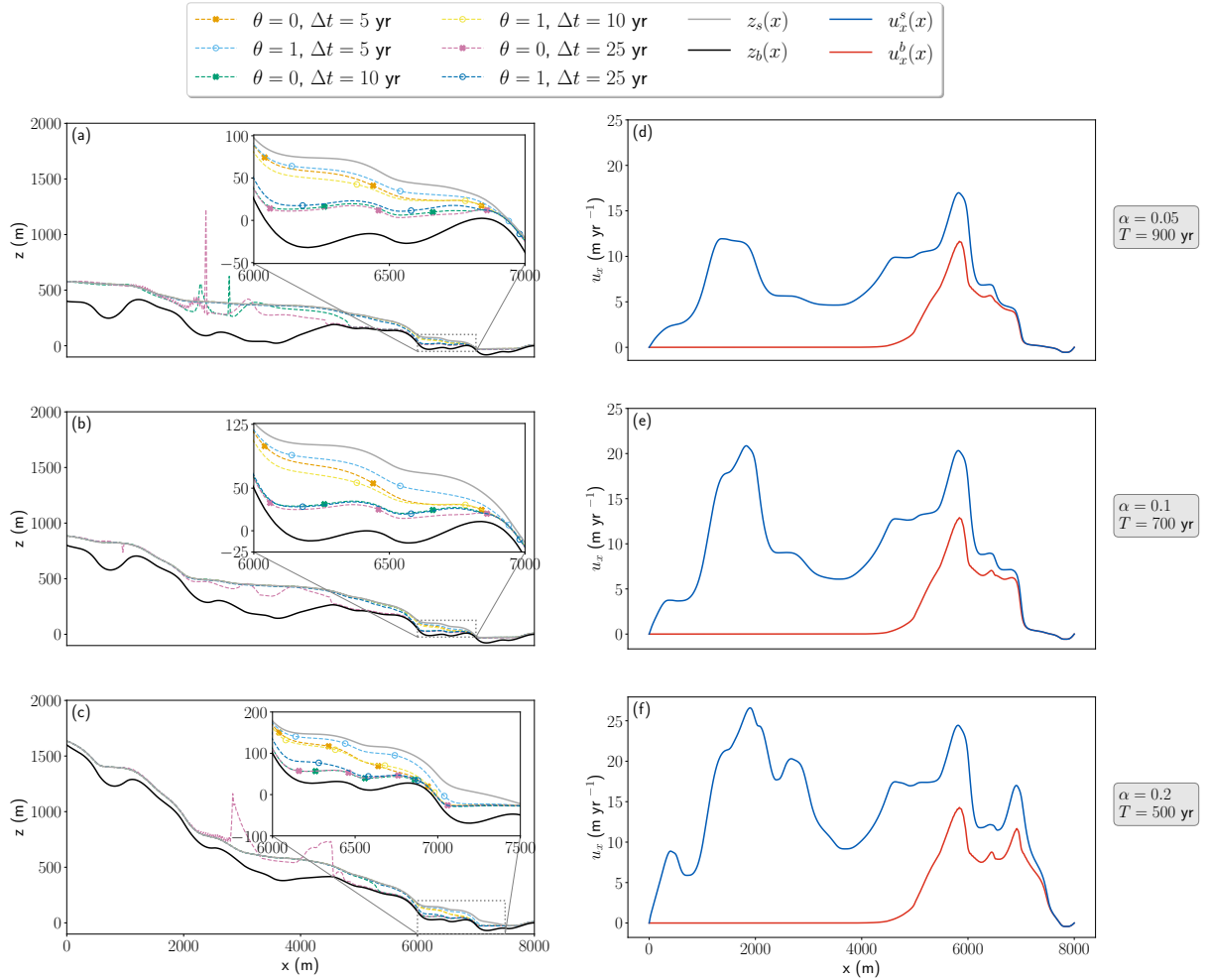| | **Ice thickness error** (%) | | | | | |
| | $\alpha = 0.05$ | | $\alpha = 0.1$ | | $\alpha = 0.2$ | |
Δt (yr)	$\theta = 0$	$\theta = 1$	$\theta = 0$	$\theta = 1$	$\theta = 0$	$\theta = 1$
0.5	0.92	0.89	1.42	1.37	1.94	1.77
1	0.97	0.90	1.43	1.30	1.95	1.51
2.5	1.45	1.19	2.72	2.12	6.42	3.89
5	2.90	2.07	6.37	4.03	15.7	8.21
10	X	3.87	13.7	7.76	33.0	15.3
25	X	8.71	X	14.8	X	24.7
50	X	14.5	X	20.4	X	42.3

Figure 3. Glacier surfaces (a-c) and horizontal velocities of the reference simulations (d-f) at final times T for different bedrock slopes α, FSSA stabilization parameters θ and time-step sizes Δt. The gray solid lines in (a-c) are the reference surface, z_s, for the respective case, and the black solid lines the bedrock, z_b. The blue solid lines in (d-f) are the surface velocities, u_x^s, and the red solid lines the bedrock slip velocities, u_x^b. The reference solution was obtained using a time-step size $\Delta t = 0.05$ yr and a fine mesh of $(N_x, N_z) = (1000, 10)$ layers and the coarse solution on mesh of $(N_x, N_z) = (400, 5)$ layers. Here N_x denotes the number of horizontal layers and N_z the number of vertical layers.
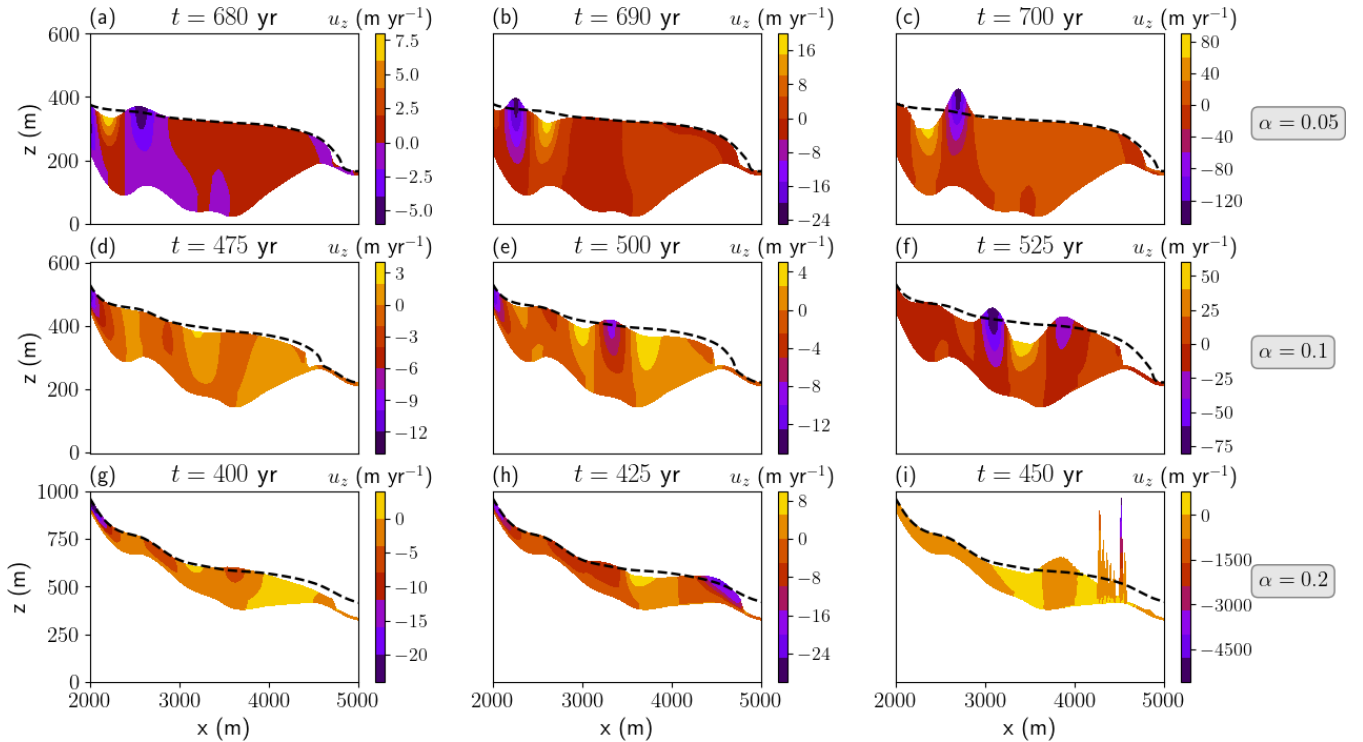
Figure 4. Vertical velocity profiles, u_z, from simulations using no FSSA ($\theta = 0$) and unstable time-step sizes $\Delta t = 10$ yr (a–c) and $\Delta t = 25$ yr (d–i) shown at the indicated times t. The profiles are shown for the different bedrock slopes $\alpha = 0.05$ yr (a–c), $\alpha = 0.1$ (d–f) and $\alpha = 0.2$ (g–i). The black dashed line in each figure is the glacier surface obtained from the stable reference simulation.

4.3 Experiment 2: Midtre Lovénbreen

4.3.1 Setup

This experiment aims to demonstrate how FSSA works for a real-world, three-dimensional glacier simulation. For this purpose, the valley glacier Midtre Lovénbreen, (78.53°N, 12.04° E) Svalbard, is chosen as it is a thoroughly studied glacier that has been modeled using Elmer/Ice previously (Zwinger and Moore, 2009; Välisuo et al., 2017). The glacier is in this study classified as an intermediate to steep sloping glacier with an average surface slope $\alpha = 0.14$ (8°). The initial geometry is shown in Fig. 5, where colors indicate ice thickness, Fig. 5a, surface mass balance (SMB), Fig. 5b, velocity magnitude, Fig. 5c, and gray contour lines represents surface heights in meters above sea level.

The basal BC is the linear sliding law of Eq. (7) with the same drag coefficient as in Välisuo et al. (2017)

$$
\beta^2(x,y,t) = \begin{cases} 0.04 \text{ MPa yr m}^{-1} & \text{if } H(x,y,t) \geq 120 \text{ m,} \\ 10 \text{ MPa yr m}^{-1} & \text{if } H(x,y,t) < 120 \text{ m,} \end{cases} \tag{21}
$$

(a) Ice thickness (colors) and surface elevation (contours)

(b) SMB (colors) and surface elevation (contours)

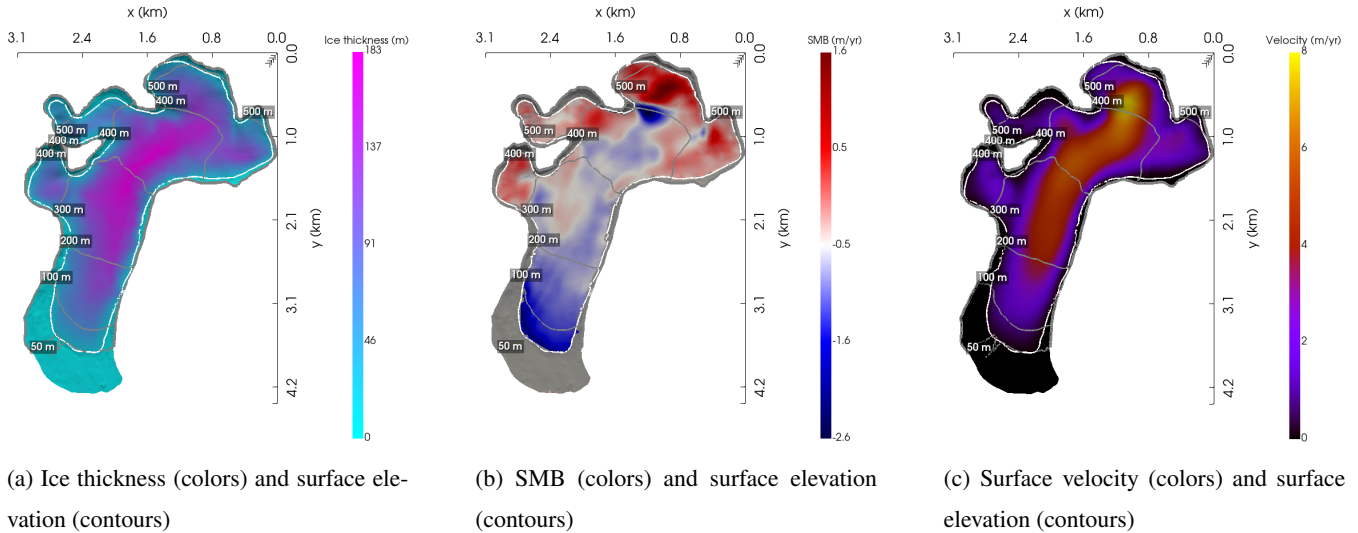(c) Surface velocity (colors) and surface elevation (contours)

Figure 5. Ice thickness, surface mass balance (SMB) excluding the deglaciated area (gray), modeled surface velocity and surface elevation of Midtre Lovénbreen at the start of the simulation, in year 1995. The ice flows from top to bottom. The computational domain is given by the 1962 extent of the glacier, the white line indicates the outline of the glacier at the start of the simulation. The figures were created using the open source visualization and analysis toolkit PyVista (Sullivan and Kaszynski, 2019).

where H is the ice thickness. This drag coefficient imposes high slip velocities at parts where the ice is thick (≥ 120 m)
285 and essentially imposes a no-slip condition at the shallower parts (< 120 m). Note that this also means that sliding velocities decrease as the glacier thins. The values for the drag coefficient were determined in Välisuo et al. (2017) by a manual inversion using observed surface velocities as input data. As in Välisuo et al. (2017), the bedrock elevation is given by a bedrock DEM created from ground-penetrating radar data (Rippin et al., 2003; Zwinger and Moore, 2009), the 1995 surface elevation DEM is based on digital photogrammetry from vertical aerial photographs, and the 2005 surface elevation DEM is a product derived
290 from airborne LIDAR (light detection and ranging) data (James et al., 2006).

Following Välisuo et al. (2017), the SMB used has been estimated from surface DEMs of the ice surface for the years 1995 and 2005. The SMB is obtained by solving the Stokes equations, Eq. (1) - (2), on the domain defined by the 1995 surface DEM, from the time-discretized free-surface equation, Eq. (11), the SMB is given by

$$a_s = \frac{z_s^{2005} - z_s^{1995}}{10 \text{ yr}} + u_x^{1995}\frac{\partial z_s^{2005}}{\partial x} + u_y^{1995}\frac{\partial z_s^{2005}}{\partial y} - u_z^{1995}. \tag{22}$$

295 The 3D mesh is generated by extruding a 2D footprint mesh into five layers ($N_z = 5$) with a horizontal resolution of about 25 m. The footprint is large enough to cover the glacier at the size it was in 1962, which implies that a large deglaciated area is included in the domain.

The glacier evolution is simulated from year 1995 to year 2195 with and without FSSA and compared and evaluated in regards to the LST and accuracy. To measure accuracy a reference solution is obtained by performing a simulation from year

14

300 1995 to 2195 using a small time-step size of $\Delta t = 1$ yr and no FSSA ($\theta = 0$). The error is estimated by comparing the ice thickness in the final solutions to the reference solution, for various time-step sizes.

To remedy convergence issues of the Newton solver (which appeared both with and without FSSA) the derivative of the viscosity appearing in the Newton linearization is relaxed by a factor two-thirds.

4.3.2 Results

305 The final glacier surface after 200 years is shown in Fig. 6a, where the color denotes the ice thickness of the reference simulation. Comparing with the thickness of the initial glacier in Fig. 5a, it is seen that the glacier surface has retreated a distance of about 1.5 km uphill. In addition the glacier has also experienced thinning from initially having a maximum thickness of about 180 m down to a maximum thickness of 100 m. The retreat of the glacier is expected given the considerably negative SMB, as can be seen from Fig. 5b. This is contrary to the 2D Perlin experiment, which considered an advancing glacier. Note, however,

310 that predicting the actual retreat of the glacier is not the objective of this study, but rather to demonstrate the stabilizing properties of the FSSA method for an SMB derived from experimental data. The true SMB is in reality likely to change substantially over the simulation period considered.

Figure 6a shows the glacier outlines for the stable reference simulation (white line), an FSSA stabilized simulation with $\Delta t = 40$ yr (dark gray line), and an unstabilized simulation with $\Delta t = 40$ yr (orange line). It is seen that the unstabilized case

315 deviates substantially from the reference simulation, due to instability, while the glacier outline from FSSA simulation is to a large extent indistinguishable from the outline of the reference simulation. The largest time-step size tested for stability in each case are shown in Table 2 where it is seen that the FSSA simulation is stable for at least twice as large time-step sizes. From Fig. 6b it is seen, similarly to the 2D Perlin experiment, that instabilities arise in the deep parts of the domain, where the error is large — indicative of the sloshing-type instability encountered in the previous experiment.

320 Figure 6c shows that for the stable time-step size $\Delta t = 20$ yr, the error using FSSA is larger than without FSSA at the deep parts of the glacier, but the accuracy near edges is higher, so that the glacier area is more accurate (top left and lower right panel). This is contrary to what was found in the previous 2D experiment, where the FSSA method was overall more accurate. The reason for this discrepancy could be explained by the fact that the estimated reference solution in this case is only refined temporally and therefore may not represent the analytical solution accurately enough. It could also be a property of the method

325 that it has higher accuracy when applied to advancing glaciers and lower accuracy for retreating glaciers. Figure 6b and Fig. 6c also show that the less accurate the solution is, the smaller the glacier retreat and larger ice thickness compared to the reference solution. This should be contrasted with the first experiment which considered an advancing glacier, where the less accurate the solution, the less the glacier had advanced.

The experiments were also run on a coarser mesh of horizontal resolution $\Delta x = 50$ m, where instabilities not present for the

330 finer mesh arose in the proximity of the small islands located around the $z_s = 50$ m contour in the deglaciated area in Fig. 6a. The instabilities took the shape of sharp spikes, similar in appearance to the instability observed at the glacier front in Fig. 4i of experiment 1. These instabilities are potentially specific to the setup and may be mitigated by other stabilization techniques

such as adding artificial diffusivity to the free-surface equation in deglaciated areas. It is, however, a positive feature of FSSA that it mitigates other instabilities than only pure sloshing instabilities.

335   In order to ensure computation times are not negatively affected by the FSSA method, an experiment was performed to measure the CPU-time of the FSSA method compared to no stabilization. The computation times for different Δt are shown in Table 3. It is seen that the FSSA method was faster for all cases. The FSSA method was about 10 % faster for the case with $\Delta t = 20$ yr, while the difference is only slightly in favor of FSSA for $\Delta t = 10$ yr and $\Delta t = 5$ yr. The difference in computation times seems to be related in this case to the average number of nonlinear iterations needed for convergence. For example, 340   for the case $\Delta t = 20$ yr the FSSA method required about 10 % fewer iterations for convergence, which explains the 10 % difference in computation times. The increase in nonlinear iterations might be due to stability issues of the unstabilized solver as the relative difference becomes smaller with decreasing Δt.

In summary, the FSSA method gave a more stable solution, increasing the LST by at least a factor of two, without negatively impacting computation times. The stabilized solver was also found to be more robust to instabilities occurring in deglaciated 345   areas. In regards to accuracy, the FSSA method yielded larger ice thickness errors in the interior, while the error was reduced at the glacier front. This has the implication that the FSSA method may be more suitable at predicting future glacier extent, while the non-FSSA method is more accurate for determining future glacier thinning.

Table 2. Largest stable time-step size of a 200 year long simulation with and without FSSA stabilization for two different mesh resolutions Δx.

	Largest stable time-step size, Midtre Lovénbreen (yr)	
	Without FSSA $\theta = 0$	With FSSA $\theta = 1$
Coarse mesh $\Delta x \sim 50$ m	20	50
Fine mesh $\Delta x \sim 25$ m	20	50

Table 3. CPU times for a 200 year long simulation for different time-step sizes Δt, measured with and without FSSA stabilization. The simulations were run on a mesh with horizontal resolution $\Delta x \sim 25$ m. Note that case with $\Delta t = 40$ yr and $\theta = 0$ is unstable.

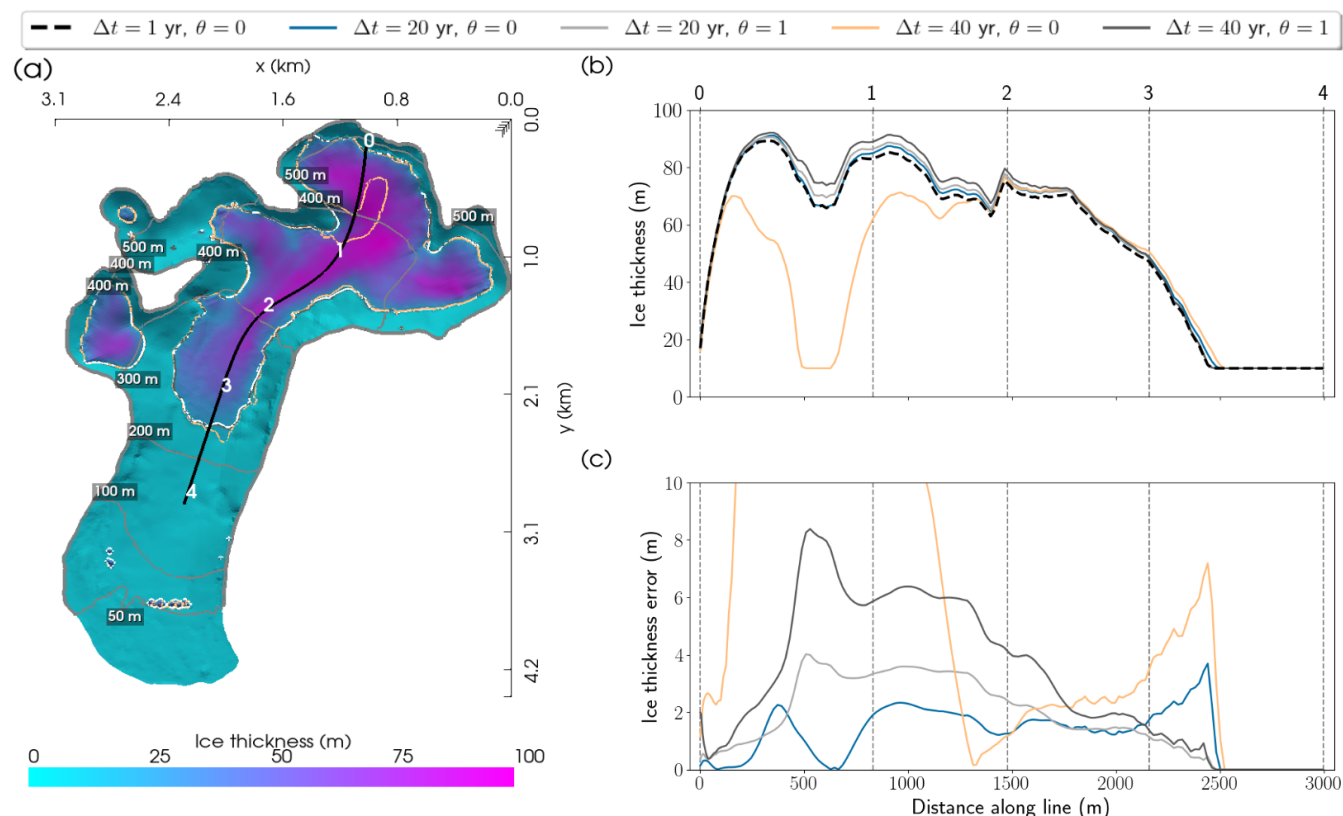|	CPU time, Midtre Lovénbreen	
Δt (yr)	Without FSSA $\theta = 0$	With FSSA $\theta = 1$
5	4h 17m	4h 14m
10	2h 20m	2h 16m
20	1h 25m	1h 15m
40	1h 1m	46m

Figure 6. Midtre Lovénbreen at year 2195. The left panel (a) shows the glacier outlines of the reference solution (white) using a fine time-step size $\Delta t = 1$ yr, as well as outlines for a simulation using a larger $\Delta t = 40$ yr, with FSSA (dark gray) and without FSSA (orange). The thickness of the glacier as given by the reference solution is indicated with colors in panel (a). The upper right panel (b) shows the ice thickness along the black line in panel (a), for the reference solution (dashed black line in (b)) and simulations with and without FSSA for $\Delta t = 20, 40$ yr (solid lines in (b)). The lower right panel (c) shows ice thickness errors as compared to the reference solution. The left panel (a) was created using the open source visualization and analysis toolkit PyVista (Sullivan and Kaszynski, 2019).

5 Conclusions

The FSSA was implemented into Elmer/Ice and tested on simulations of synthetic glaciers as well as on Midtre Lovénbreen, Svalbard. The FSSA increased the largest stable time-step (LST) size by a factor of two for the simulation of Midtre Lovénbreen and by a factor of ten in the synthetic glacier with low surface slope. The LST for the unstabilized method was, however, already quite large for all simulations (5 to 30 yrs), unlike for the ice-sheet simulations in Löfgren et al. (2022). Low glacier surface slopes were correlated with shorter time-step sizes for the unstabilized method and were also the cases where the stabilization had the greatest effect. This may be due to the large ice thickness of glaciers with low bedrock inclination, leading to a more viscous behavior of the problem.

The FSSA mitigated instabilities of different natures (sloshing instabilities, spikes in deglaciated areas) and thereby improved robustness of simulations. Somewhat unexpectedly, the accuracy was also overall improved (except for in deep parts of Midtre Lovénbreen). As the computational cost is also low, this leads us to draw the conclusion that FSSA can be added as a security measure in simulations to prevent unexpected convergence issues (crashes) of simulations without compromising the result or

360   simulation times. For glacier simulations this may offer the greatest benefit of FSSA, given the already large time-step sizes of the unstabilized method. Another potential usage are spin-up simulations, where a very large time-step size of e.g., 50 yr could be used. Climate data could then be incorporated on shorter time scales using semi-implicit time stepping of the surface.

In the previous study by Löfgren et al. (2022) the FSSA was tested on synthetic ice-sheet experiments, largely disregarding the effect of variable bedrock and sliding conditions and simplifying the contact problem near glacier fronts. This paper

365   demonstrates that the FSSA method is applicable for more complex real-world simulations and the new implementation in Elmer/Ice makes the method accessible to a broad user base.

Code availability. Elmer version `fededfbf7` (branch `devel`) has been used in this study and is downloadable from https://github.com/ElmerCSC/elmerfem.

Appendix A: Bedrock generation

370   This section presents an algorithm that is used to random-generate bedrock topographies. It is based on a method that is common practice in computer graphics as a computationally inexpensive and flexible way of random generating visually appealing landscapes, clouds, textures etc., known as gradient noise. The first application of gradient noise, so-called Perlin noise, was developed by Perlin (1985) to model fire, water and wrinkled surfaces, and later adapted by Musgrave et al. (1989) for landscape generation. As the name suggests, gradient noise is based on generating a set of pseudo-random gradients at

375   predefined vertices and then interpolating polynomials matching these gradients, such that the resulting global interpolating function is smooth. In this study, the mesh vertices are assumed to be equally spaced with a spatial period Δx^f. The superscript f is used to denote the fact that the final noise function may consist of multiple spatial frequencies, so-called *octaves* — similar to a Fourier decomposition. See Fig. A1 for an example of a random-generated bedrock consisting of three octaves.

For the interpolation, cubic and bicubic Hermite interpolation is used in 2D and 3D, respectively, such that

380
$$p^k(x) = \sum_{i=0}^{3} c_i x^j \tag{A1}$$

$$p^k(x,y) = \sum_{i=0}^{3} \sum_{j=0}^{3} c_{ij} x^i y^j \tag{A2}$$

where p^k is the polynomial interpolation in cell k, and c_i (or c_{ij} in 3D) are coefficients determined by matching gradients and function values at the vertices. This gives the set of equations for each vertex $\mathbf{x_i}$ in cell k

$$p^k(\mathbf{x}_i) = 0, \tag{A3}$$

$$\frac{\partial p^k(\mathbf{x}_i)}{\partial x} = f_{x_i}, \tag{A4}$$

$$\frac{\partial p^k(\mathbf{x}_i)}{\partial y} = f_{y_i}, \tag{A5}$$

$$\frac{\partial^2 p^k(\mathbf{x}_i)}{\partial x \partial y} = f_{xy_i}, \tag{A6}$$

where f_{x_i}, f_{y_i} and f_{xy_i} are the components of the random generated gradients. Since the number of vertices in each cell in 2D are two and four in 3D, this leads to a total of four equations in 2D and 16 equations in 3D, matching the total number of unknowns for the respective cases. Solving the resulting linear system then gives the octave characterized by the spatial period Δx^f of the noise function. The final noise function is obtained by summing all the octaves, such that

$$\text{noise}(x,y) = \sum_{f=1}^{n} A^f \text{octave}(\Delta x^f, x, y) \tag{A7}$$

where A^f and Δx^f are the amplitude and spatial period of the f:th octave, respectively, and n is the number of octaves.

Competing interests. JA is a member of the editorial board of The Cryosphere. The peer-review process was guided by an independent editor, and the authors have also no other competing interests to declare.
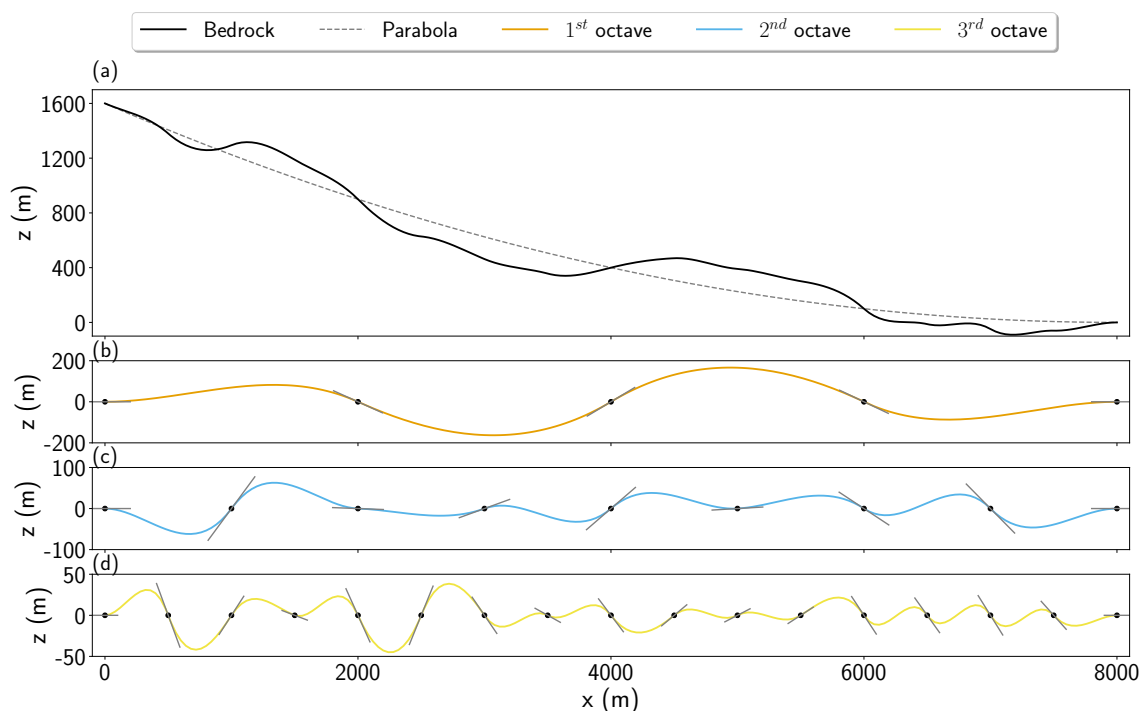
19

Figure A1. Gradient noise consisting of three octaves (orange, blue and yellow solid lines in (b–d)) superimposed on a parabola (gray dashed line in (a)) to generate a naturally looking bedrock topography (black solid line in (a)). Spatial periods of the octaves (b–d) are $\Delta x^1 = 2000$ m (orange solid line in (b)), $\Delta x^2 = 1000$ m (blue solid line in (c)) and $\Delta x^3 = 500$ m (yellow solid line in (d)). The black dots and gray solid lines in (b–d) denote the nodal values (zero in this case) and the matched pseudo-random generated tangents.

References

Andrés-Martínez, M., Morgan, J. P., Pérez-Gussinyé, M., and Rüpke, L.: A new free-surface stabilization algorithm for geodynamical mod-

410 elling: Theory and numerical tests, Phys. Earth Planet. In., 246, 41–51, https://doi.org/10.1016/j.pepi.2015.07.003, 2015.

Blatter, H.: Velocity and stress fields in grounded glaciers: a simple algorithm for including deviatoric stress gradients, J. Glaciol., 41, 333–344, https://doi.org/10.1017/S002214300001621X, 1995.

Blatter, H., Greve, R., and Abe-Ouchi, A.: A short history of the thermomechanical theory and modelling of glaciers and ice sheets, J. Glaciol., 56, 1087–1094, https://doi.org/https://doi.org/10.3189/002214311796406059, 2010.

415 Bueler, E.: Stable finite volume element schemes for the shallow-ice approximation, J. Glaciol., 62, 230–242, 2016.

Bueler, E.: Performance analysis of high-resolution ice-sheet simulations, J. Glaciol., pp. 1–6, https://doi.org/10.1017/jog.2022.113, 2022.

Bueler, E., Lingle, C. S., Kallen-Brown, J. A., Covey, D. N., and Bowman, L. N.: Exact solutions and verification of numerical models for isothermal ice sheets, J. Glaciol., 51, https://doi.org/10.3189/172756505781829449, 2005.

Cuffey, K. M. and Paterson, W. S. B.: The Physics of Glaciers, Butterworth-Heinemann, Amsterdam, 4th edn., 2010.

420 DeConto, R. M. and Pollard, D.: Contribution of Antarctica to past and future sea-level rise, Nature, 531, 591–597, https://doi.org/10.1038/nature17145, 2016.

Dukowicz, J. K., Price, S. F., and Lipscomb, W. H.: Incorporating arbitrary basal topography in the variational formulation of ice-sheet models, J. Glaciol., 57, 461–467, https://doi.org/10.3189/002214311796905550, 2011.

Duretz, T., May, D. A., Gerya, T. V., and Tackley, P. J.: Discretization errors and free surface stabilization in the finite difference and marker-
425 in-cell method for applied geodynamics: A numerical study, Geochem. Geophy. Geosy., 12, https://doi.org/10.1029/2011GC003567, 2011.

Fox-Kemper, B., Hewitt, H., Xiao, C., Aðalgeirsdóttir, G., Drijfhout, S., Edwards, T., Golledge, N., Hemer, M., Kopp, R., Krinner, G., Mix, A., Notz, D., Nowicki, S., Nurhati, I., Ruiz, L., Sallée, J.-B., Slangen, A., and Yu, Y.: Ocean, Cryosphere and Sea Level Change, pp. 1211––1362, Cambridge University Press, Cambridge, United Kingdom and New York, NY, USA, https://doi.org/10.1017/9781009157896.011, 2021.

430 Gagliardini, O., Zwinger, T., Gillet-Chaulet, F., Durand, G., Favier, L., de Fleurian, B., Greve, R., Malinen, M., Martín, C., Råback, P., Ruokolainen, J., Sacchettini, M., Schäfer, M., Seddik, H., and Thies, J.: Capabilities and performance of Elmer/Ice, a new generation ice-sheet model, Geoscientific Model Development, 6, 1299–1318, https://doi.org/10.5194/gmdd-6-1689-2013, 2013.

Glen, J. W.: The Creep of Polycrystalline Ice, P. R. Soc. London, 228, 519–538, https://doi.org/10.1098/rspa.1955.0066, 1955.

Glerum, A., Brune, S., Stamps, D. S., and Strecker, M. R.: Victoria continental microplate dynamics controlled by the lithospheric strenght
435 distribution of the East African Rift, Nat. Commun., 11, 2881, https://doi.org/10.1038/s41467-020-16176-x, 2020.

Gong, C., Lötstedt, P., and von Sydow, L.: Accurate and stable time stepping in ice sheet modeling, J. Comput. Phys, 329, 29–47, https://doi.org/10.1016/j.jcp.2016.10.060, 2017.

Greve, R. and Blatter, H.: Dynamics of Ice Sheets and Glaciers, Advances in Geophysical and Environmental Mechanics and Mathematics, Springer-Verlag Berlin Heidelberg, https://doi.org/10.1007/978-3-642-03415-2, 2009.

440 Hanna, E., Navarro, F. J., Pattyn, F., Domingues, C. M., Fettweis, X., Ivins, E. R., Nicholls, R. J., Ritz, C., Smith, B., Tulaczyk, S., White-house, P. L., and Zwally, H. J.: Ice-sheet mass balance and climate change, Nature, 498, https://doi.org/10.1038/nature12238, 2013.

Hindmarsh, R. C. A. and Payne, A. J.: Time-step limits for stable solutions of the ice-sheet equation, Ann. Glaciol., 23, 74–85, https://doi.org/10.3189/S0260305500013288, 1996.

Hock, R., Bliss, A., Marzeion, B., Giesen, R. H., Hirabayashi, Y., Huss, M., Radić, V., and Slangen, A. B. A.: GlacierMIP – A model in-
445 tercomparison of global-scale glacier mass-balance models and projections, J. Glaciol., 65, 453–467, https://doi.org/10.1017/jog.2019.22, 2019.

Hutter, K.: Theoretical Glaciology: Material Science of Ice and the Mechanics of Glaciers and Ice Sheets, Mathematical Approaches to Geophysics 1, D. Reidel Publishing Company, Dordrecht, Holland and Terra Scientific Publishing Company, Tokyo, Japan, 1983.

James, T. D., Murray, T., Barrand, N. E., and Barr, S. L.: Extracting photogrammetric ground control from lidar DEMs for change detection,
450 The Photogrammetric Record, 21, 312–328, 2006.

Kaus, B. J., Mühlhaus, H., and May, D. A.: A stabilization algorithm for geodynamic numerical simulations with a free surface, Phys. Earth Planet. In., 181, 12–20, https://doi.org/10.1016/j.pepi.2010.04.007, 2010.

Kramer, S. C., Wilson, C. R., and Davies, D. R.: An implicit free surface algorithm for geodynamical simulations, Phys. Earth Planet. In., 194-195, 25–37, https://doi.org/10.1016/j.pepi.2012.01.001, 2012.

455 Leng, W., Ju, L., Gunzburger, M., Price, S., and Ringler, T.: A parallel high-order accurate finite element nonlinear Stokes ice sheet model and benchmark experiments, J. Geophys. Res., 117, https://doi.org/10.1029/2011JF001962, 2012.

Löfgren, A., Ahlkrona, J., and Helanow, C.: Increasing stable time-step sizes of the free-surface problem arising in ice-sheet simulations, J. Comput. Phys. X, 16, https://doi.org/10.1016/j.jcpx.2022.100114, 2022.

Meredith, M., Sommerkorn, M., Cassotta, S., Derksen, C., Ekaykin, A., Hollowed, A., Kofinas, G., Mackintosh, A., Melbourne-Thomas,
460   J., Muelbert, M., Ottersen, G., Pritchard, H., and Schuur, E.: IPCC Special Report on the Ocean and Cryosphere in a Changing Climate, chap. Polar Regions, pp. 203–320, Cambridge University Press, https://doi.org/10.1017/9781009157964.005, 2019.

Meur, E. L., Gagliardini, O., Zwinger, T., and Ruokolainen, J.: Glacier flow modelling: a comparison of the Shallow Ice Approximation and the full-Stokes solution, C. R. Phys., 5, 709–722, https://doi.org/10.1016/j.crhy.2004.10.001, 2004.

Morland, L. W.: Thermomechanical balances of ice sheet flows, Geophys. Astro Fluid, 29, 237–266,
465   https://doi.org/10.1080/03091928408248191, 1984.

Musgrave, F. K., Kolb, C. E., and Mace, R. S.: The Synthesis and Rendering of Eroded Fractal Terrain, ACM SIGGRAPH Comput. Graph., 23, https://doi.org/10.1145/74334.74337, 1989.

Nye, J. F.: The distribution of stress and velocity in glaciers and ice-sheets, Proc. R. Soc. Lon. Ser-A, 239, 113–133, https://doi.org/10.1098/rspa.1957.0026, 1957.

470 Paterson, W. S. B.: The Physics of Glaciers, Elsevier Science Ltd, The Boulevard, Langford Lane, Kidlington, Oxford, 3rd edn., https://doi.org/10.1016/C2009-0-14802-X, 1994.

Pattyn, F.: A new three-dimensional higher-order thermomechanical ice sheet model: Basic sensitivity, ice stream development, and ice flow across subglacial lakes, J. Geophys. Res., 108, https://doi.org/10.1029/2002JB002329, 2003.

Pattyn, F.: The paradigm shift in Antarctic ice sheet modelling, Nat. Commun., 9, 2728, https://doi.org/10.1038/s41467-018-05003-z, 2018.

475 Perlin, K.: An Image Synthesizer, ACM SIGGRAPH Comput. Graph., 19, 287–296, https://doi.org/10.1145/325165.325247, 1985.

Rippin, D., Willis, I., Arnold, N., Hodson, A., Moore, J., Kohler, J., and Björnsson, H.: Changes in geometry and subglacial drainage of Midre Lovénbreen, Svalbard, determined from digital elevation models, Earth Surf. Proc. Land., 28, 273–298, https://doi.org/https://doi.org/10.1002/esp.485, 2003.

Robinson, A., Goldberg, D., and Lipscomb, W. H.: A comparison of the stability and performance of depth-integrated ice-dynamics solvers,
480   The Cryosphere, 16, 689–709, https://doi.org/10.5194/tc-16-689-2022, 2022.

Rose, I., Buffet, B., and Heister, T.: Stability and accuracy of free surface time integration in viscous flows, Phys. Earth Planet. In., 262, 90–100, https://doi.org/j.pepi.2016.11.007, 2017.

Shepherd, A. and Nowicki, S.: Improvements in ice-sheet sea-level projections, Nat. Clim. Change, 7, 672–674, https://doi.org/10.1038/nclimate3400, 2017.

485 Sullivan, C. B. and Kaszynski, A.: PyVista: 3D plotting and mesh analysis through a streamlined interface for the Visualization Toolkit (VTK), Journal of Open Source Software, 4, 1450, https://doi.org/10.21105/joss.01450, 2019.

Välisuo, I., Zwinger, T., and Kohler, J.: Inverse solution of surface mass balance of Midtre Lovénbreen, Svalbard, J. Glaciol., 63, 593—602, https://doi.org/10.1017/jog.2017.26, 2017.

Weertman, J.: On the sliding of glaciers, J. Glaciol., 3, 38–42, https://doi.org/10.3189/S0022143000024709, 1957.

490 Zwinger, T. and Moore, J. C.: Diagnostic and prognostic simulations with a full Stokes model accounting for superimposed ice of Midtre Lovénbreen, Svalbard, The Cryosphere, 3, 217–229, https://doi.org/10.5194/tc-3-217-2009, 2009.

Zwinger, T., Greve, R., Gagliardini, O., Shiraiwa, T., and Lyly, M.: A full Stokes-flow thermo-mechanical model for firn and ice applied to the Gorshkov crater glacier, Kamchatka, Ann. Glaciol., 45, 29–37, https://doi.org/10.3189/172756407782282543, 2007.